RSC Advances

PAPER

View Article Online
View Journal | View Issue

Cite this: *RSC Adv.*, 2015, **5**, 56279

Hydrothermal synthesis of hierarchical core–shell manganese oxide nanocomposites as efficient dye adsorbents for wastewater treatment†

Wei Wang,[ab] Tifeng Jiao,*[abc] Qingrui Zhang,*[b] Xiaona Luo,[b] Jie Hu,[b] Yan Chen,[b] Qiuming Peng,[a] Xuehai Yan[c] and Bingbing Li*[d]

Received 10th May 2015
Accepted 22nd June 2015

DOI: 10.1039/c5ra08678g

www.rsc.org/advances

In this work, hierarchical core–shell manganese oxide nanocomposites (Fe_3O_4@MnO_2 and Fe_2O_3@MnO_2) were synthesized *via* a facile hydrothermal process without using any templates or organic surfactants. The effect of reaction time on the microstructure and morphology of composite samples was systemically investigated. The formation mechanism of the core–shell structure was carefully analyzed by using field emission scanning electron microscopy (FESEM), transmission electron microscopy (TEM), and Brunauer–Emmett–Teller (BET) surface area measurement. Both nitrogen adsorption–desorption experiments and morphological study showed that the composite obtained through 6 hour hydrothermal reaction has fairly large specific surface area, uniform pore-size distribution, and good adsorption capability. The dye adsorption experiments further demonstrated the potential applications of the manganese oxide nanocomposites as efficient dye adsorbents for wastewater treatment.

1. Introduction

In recent years, water pollution has exerted negative effects not only on species living in the water but also on the broader biological community. For instance, organic dyes are often discharged with wastewater into the local environment without adequate treatment. Rapid and convenient removal of organic dyes from wastewater has been a challenging issue faced by scientists.[1–4] In particular, large-scale application requires the potential dye adsorbents to exhibit high dye removal rate within a relatively short period of time and to be environmentally friendly. In comparison to other adsorbents under investigation, nanostructured adsorbents exhibit remarkably enhanced sorption capacity owing to their high surface-to-volume ratio. During the last decades, various nanosized adsorbents have been prepared and adopted for water decontamination.[5–8] However, such nanomaterials still suffer from issues involving separation inconvenience from the wastewater. Thus, the development of new nanostructured adsorbents with a facile separation property is of great interest.[9–11] In order to achieve this purpose, iron oxide nanoparticles, in particular magnetite (Fe_3O_4) and maghemite (γ-Fe_2O_3), have been extensively applied in designing nanocomposite adsorbents because they have a large surface area and high magnetic susceptibility.[12] These nanoparticles are attracted to an external magnetic field but lose magnetism as the applied field is removed, which allows their fast and convenient isolation in the processing and recovery stages. In the past years, research has been conducted to functionalize magnetic nanoparticles by coating them with inorganic materials, polymers, biomolecules, *etc.*[13–19] Surface functionalization has been found to enhance the stability and sorption capacity of magnetic nanocomposites. Thus, it is highly important to develop new functional composite materials that can further enhance the adsorption property of pristine magnetic nanoparticles while exhibit a low-cost and environmentally benign nature. Nanostructured manganese oxides (MnO_2) are among the most reactive minerals that have a high surface area, strong adsorption ability, and good stability.[20] Therefore, the modification of the Fe_3O_4 surface with MnO_2 to form core–shell nanostructure is anticipated to increase the removal efficiency of the magnetic nanoparticles for environmental applications.[21–23] For example, Zhu *et al.* reported the preparation of new composite adsorbent by combining honeycomb briquette cinders (HBC) with Fe_3O_4 and MnO_2 through a co-precipitation process and the applications of the prepared nanocomposites for As(III) and As(V) removal from aqueous solutions under different experimental

[a]*State Key Laboratory of Metastable Materials Science and Technology, Yanshan University, Qinhuangdao 066004, P. R. China. E-mail: tfjiao@ysu.edu.cn*

[b]*Hebei Key Laboratory of Applied Chemistry, School of Environmental and Chemical Engineering, Yanshan University, Qinhuangdao 066004, P. R. China. E-mail: zhangqr@ysu.edu.cn*

[c]*National Key Laboratory of Biochemical Engineering, Institute of Process Engineering, Chinese Academy of Sciences, Beijing 100190, P. R. China*

[d]*Department of Chemistry and Biochemistry, Science of Advanced Materials Doctoral Program, Central Michigan University, Mount Pleasant, MI 48859, USA. E-mail: li3b@cmich.edu*

† Electronic supplementary information (ESI) available: Physical properties deduced from N_2 adsorption was presented in Table S1. The kinetic data for fitting was presented in Table S2. See DOI: 10.1039/c5ra08678g

conditions.[22] By taking advantage of the Fe_3O_4 core and MnO_2 shell, along with the mesoporous structure of the composites, MnO_2-coated Fe_3O_4 nanoparticles could be an ideal material with a great potential for environmental remediation. Although previous research has highlighted the advantages of MnO_2 coating for metal-ion adsorption,[24,25] they looked into the sorption percentage without an in-depth investigation into the mechanism and experimental parameters. In addition, no previous study has focused on the comparison of MnO_2-coated magnetic or non-magnetic particles for wastewater treatment.

In this study, hierarchically structured core–shell manganese oxide nanocomposites (magnetic Fe_3O_4@MnO_2 and non-magnetic Fe_2O_3@MnO_2) were successfully synthesized. The morphologies and structures of the composite materials were investigated by various characterization methods, including SEM, TEM, and XRD. The obtained composites were used to adsorb different dyes, for examples, methylene blue (MB) and rhodamine B (RhB) from aqueous systems. The overall performance of nanocomposites was assessed in terms of sorption kinetics.

2. Materials and methods

2.1 Materials

All the used chemical reagents, Potassium Permanganate ($KMnO_4$, AR, Aladdin reagent Co., Ltd), ferric chloride ($FeCl_3 \cdot 6H_2O$, AR, Aladdin reagent Co., Ltd), ammonium hydroxide ($NH_3 \cdot H_2O$, AR, Tianjin Fangzheng reagent factory), acetic acid (CH_3COOH, AR, Tianjin kemiou chemical reagent Co., Ltd) and ethylene glycol, were of analytical grade and used without further purification. Rhodamine B and methylene blue were obtained from Beijing Chemicals (analytical reagent grade, Beijing, China). All other solvents and reagents used in this study were purchased from Sinopharm Chemical Reagent Co. Ltd (analytical reagent grade, Shanghai, China). The deionized (DI) water was obtained using a Millpore Milli-Q water purification system with a resistivity of 18.2 MΩ cm^{-1}. All chemicals were used as received without further purification.

2.2 Fabrication of core–shell nanocomposites

(a) Synthesis of Fe_3O_4 nanoparticles. Fe_3O_4 nanoparticles used in this study were prepared by a modified solvothermal method.[26] Ferric chloride hexahydrate (1.35 g) was first dissolved in 30 mL ethylene glycol, followed by adding sodium hydroxide (1.0 g) and polyethylene glycol (1.0 g) into the solution mixtures. After stirring for 30 minutes, the mixture solutions were transferred into a Teflon-lined stainless steel autoclave (100 mL) and reacted at 200 °C for 8 hours. After the reaction was complete, the black precipitate (*i.e.*, the Fe_3O_4 nanoparticles) was collected by an external magnetic field, followed by alternatively washing with deionized water and ethanol for several times. Finally, the Fe_3O_4 nanoparticles were dried at 60 °C in a vacuum oven.

(b) Synthesis of Fe_2O_3 nanoparticles. In a modified reaction process for the synthesis of α-Fe_2O_3 nanoparticles,[27] 0.0025 mol $FeCl_3 \cdot 6H_2O$ solid were added into 50 mL ultrapure water under magnetic stirring at 60 °C. Until it was completely dissolved, $NH_3 \cdot H_2O$ was dropwise added into the solution to make the mixed solution of pH 11 and continue to stir for 30 min. Subsequently, a crystal shape control agent, acetic acid with concentration of 0.15 mol L^{-1} was added into the above solution. After stirring, the resultant solution was loaded into a Teflon-lined stainless steel autoclave, which was then sealed and heated up to 160 °C for 24 h. After completing the reaction, the autoclave was naturally cooled at room-temperature and finally the product was obtained, which was washed with deionized water and ethanol sequentially and then dried at 60 °C in a vacuum oven.

(c) Fabrication of Fe_3O_4@MnO_2 and Fe_2O_3@MnO_2 nanocomposites. Core–shell manganese oxide nanocomposites were prepared *via* a modified hydrothermal process.[28] Typically, 0.51 g of $KMnO_4$ was first dissolved in 35 mL of DI water, followed by dropwise adding 0.7 mL of HCl (37 wt%) solution. After stirring for 15 min, 0.3 g of Fe_3O_4 or Fe_2O_3 particles were added into the solution, respectively. The mixture was then transferred to a Teflon-lined autoclave (50 mL), which was sealed and heated at 110 °C for different times. Finally, the obtained products were washed with DI water and ethanol sequentially and dried in a lyophilizer under vacuum at −50 °C for 2 to 3 days.

2.3 Dye adsorption and composite regeneration experiments

The dye adsorption capacity of hybrid materials was probed using an absorption spectroscopy. Typically, about 100 mg of nanocomposites was added to either 100 mL of MB (10 mg L^{-1}) or 50 mL of RhB (4 mg L^{-1}) solutions. Above dye solutions containing nanostructured adsorbents were stirred at room temperature. The gel samples were then separated by centrifugation at different time intervals and the supernatant liquid was collected for subsequent analysis using an UV-vis spectrometer (752, Sunny Hengping, Shanghai, China). The absorbance at 664 nm for MB or 554 nm for RhB was used to determine the concentration of residual dyes in the supernatant liquid. Once saturated adsorption for a given dye in an aqueous suspension was reached after 12 h in a shaking table at 25 °C, the Fe_3O_4@MnO_2 nanocomposite was extracted from the solution through external magnetic attraction, and washed alternatively using ethylene glycol and ethanol for several times. Finally, the regenerated core–shell composites were then washed by DI water and dried in a lyophilizer for subsequent adsorption experiments.

2.4 Characterization

Core–shell nanocomposites were obtained by lyophilizing at −50 °C *via* a lyophilizer (FD-1C-50, Beijing Boyikang Experimental Instrument Co., Ltd., China) to completely remove water over 2 to 3 days. The size and morphology of the products were characterized by using both a field-emission scanning electron microscopy (S-4800II, Hitachi, Japan; SUPRA 55 SAPPHIRE, CARL ZEISS (Shanghai), Co., Ltd) with a accelerating voltage of 5–15 kV and a transmission electron microscopy (TEM, HT7700, Hitachi High-Technologies Corporation) with commercial 300 mesh copper grids. The chemical composition of the samples

was characterized by energy-dispersive X-ray spectroscopy (EDXS). EDXS analysis was typically performed at an accelerating voltage of 200 kV, using an Oxford Link-ISIS X-ray EDXS microanalysis system attached to TEM. X-ray diffraction study was carried out by using an X-ray diffractometer (SMART LAB, Rigaku) equipped with a conventional Cu Kα X-ray radiation (λ = 1.54 Å) source and a Bragg diffraction setup. The Brunauer–Emmett–Teller (BET) surface area and pore size distributions were measured by N_2 adsorption and desorption using an ASAP 2010 system at 77 K. The magnetic properties of the samples were tested by a vibrating sample magnetometer (VSM) of the Physical Property Measurement System (PPMS, Quantum design Model 6000). The powders were aligned under a 10 kOe field and solidified with epoxy resin for the VSM measurements.

3. Results and discussion

Fig. 1 displays typical SEM images of the as-prepared nanostructures. The SEM image shown in Fig. 1a gives a panoramic morphology of the MnO_2 sample, revealing that the product is composed of many uniform siberian cocklebur-like architectures with 3–4 μm diameter. Further observation indicated that the formed structure was covered by many needle-like aggregates. It should be noted that the size of nanoparticles was evaluated by averaging 50 particles observed in different images. In addition, two types of nanoparticles (Fe_3O_4 and Fe_2O_3) have been prepared as the cores of the designed nanocomposites. As shown in Fig. 1b and c, the ranges of particle diameters were about 80–100 nm and 150–200 nm, respectively. Subsequently, two types of nanocomposites, *i.e.*, Fe_3O_4@MnO_2 and Fe_2O_3@MnO_2 were prepared and investigated. In order to understand the effect of reaction time on the microstructure and morphology of samples, time-dependent experiments in hydrothermal reaction were carried out and the resultant products were analyzed at time of 3 h, the obtained MnO_2 sample has a spherical morphology with 2.5–3 μm diameter. The SEM image (Fig. 1d) demonstrates that the composites are covered by many interleaving thin nanoplates. These nanoplates seemed to grow perpendicularly from a center. With increasing the reaction time to 6 h, the diameter of flower-like structures changed to about 4 μm with similar morphology. When reaction time reached 9 h, the spherical structures merged together, leaving little holes or defects. Finally, the aggregates continuously grew in size to form hollow urchin-like structures with visible cavities after 15 h (Fig. 1g). In addition, Fe_2O_3@MnO_2 nanocomposite achieved after 6 h reaction was also prepared, as shown in Fig. 1h. Uniform siberian cocklebur-like structures with a 2–3 μm diameter and partially non-coated

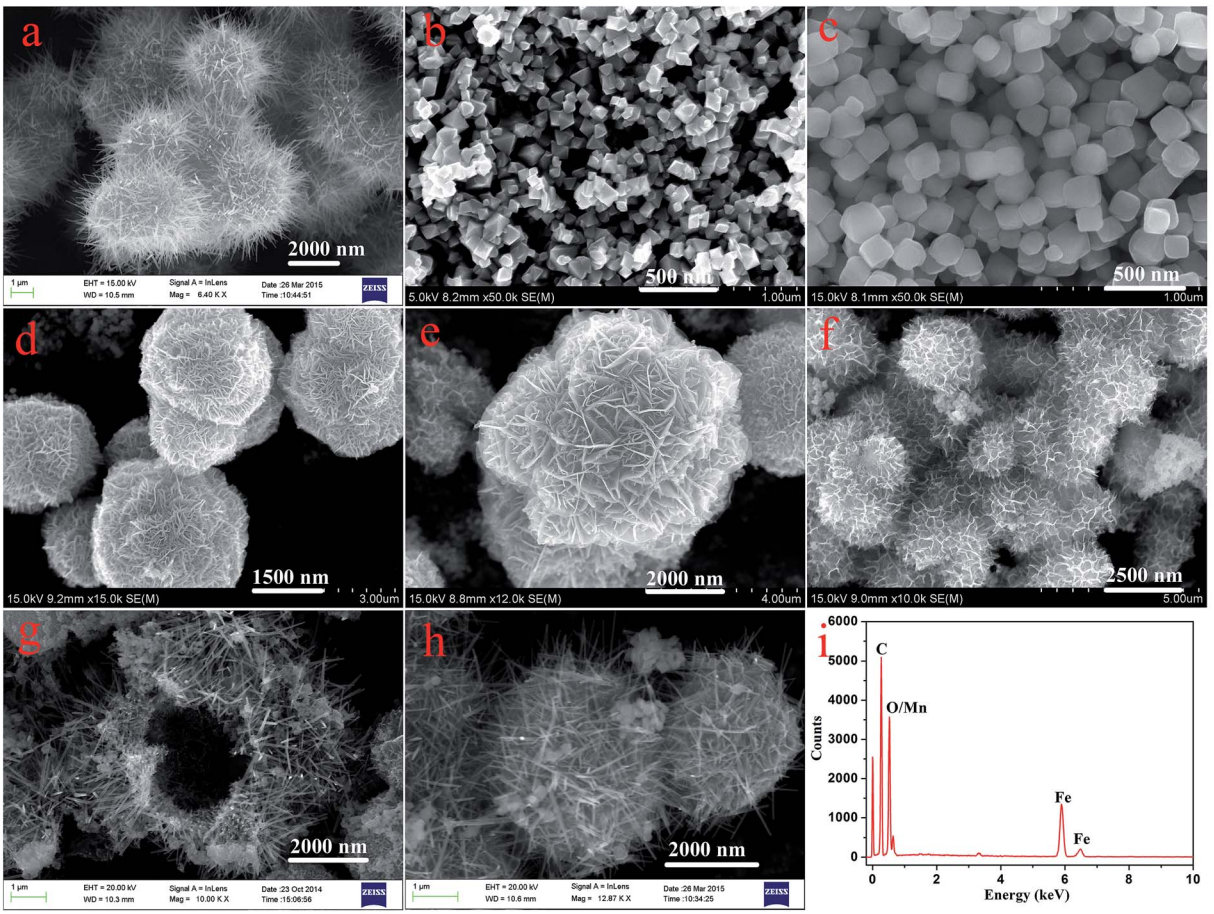

Fig. 1 SEM images of as-prepared nanostructures. (a) MnO_2; (b) Fe_3O_4; (c) Fe_2O_3; (d)–(g) Fe_3O_4@MnO_2 prepared at times of 3 h, 6 h, 9 h, and 15 h, respectively; (h) Fe_2O_3@MnO_2 prepared at time of 6 h; (i) typical EDXS of Fe_3O_4@MnO_2 nanocomposites prepared at 6 h.

Fe_2O_3 nanoparticles were also clearly observed. In addition, the typical EDXS of Fe_3O_4@MnO_2 nanocomposites prepared at 6 h showed the existence of Fe and Mn elements, also confirming the successful preparation of the composite materials. The above time-dependent morphological evolution could be correlated to an "Ostwald ripening process".[29–31] During the reaction process, a large number of nuclei are first formed in a short period of time through a well-known "Ostwald ripening process", followed by a slow crystal growth process. The aggregates continuously grow in size and density to form spheres with solid cores. This stage could last for several hours, and then an interior cavity is gradually formed *via* a core evacuation process due to higher surface energies. A subsequent increase in the hydrothermal time not only leads to the complete damage of the urchin structure but also increases the size of the individual nanorods, which confirms that Ostwald ripening is the underlying mechanism in this hollowing process. Such a core evacuation process is also observed in the similar synthesis of titania and NiO hollow spheres.[32,33] Present experimental results also reveal that 6 h would be enough for the nanocomposites to reach their equilibrium size of flower-like structures. In addition, the interesting morphology and the above microstructures was further studied using TEM technique, as shown in Fig. 2. Several obvious stages of morphological evolution could be clearly observed for Fe_3O_4@MnO_2 nanocomposites prepared at different times. The TEM image in Fig. 2f further confirmed that the Fe_3O_4@MnO_2 nanocomposites obtained after 15 h hydrothermal reaction were composed of intercrossed nano-needles. It should be noted that the TEM samples were prepared on copper grids and the obtained lyophilized core–shell nanocomposites were ultrasonated in water for several minutes and dropped on copper grid carefully. So the dispersion of nanocomposites in TEM images seems not very well and the core–shell structures could exhibit deformation in TEM images. Neverless, the above results strongly indicate that the reaction time plays an important role for the fabrication of core–shell structured MnO_2 nanocomposites.

XRD patterns of bare MnO_2 and as-prepared nanocomposites are shown in Fig. 3. Firstly, the characteristic peaks of bare MnO_2 material is in well accordance with the standard card (PDF#72-1982). In addition, the curves of the prepared Fe_3O_4 and Fe_2O_3 nanoparticles were face centered cubic phases (PDF#88-0315 and PDF#89-0599). As for the obtained two kinds of nanocomposites, the results demonstrated that increasing MnO_2 coating did not result in a phase change in the structure of the Fe_3O_4 and Fe_2O_3 nanoparticles. The newly appeared peaks for the samples obtained with prolonged reaction time can be attributed to the crystalline nature of MnO_2 structures in outer shell layers. The large surface area and mesoporous structures of the obtained composites make them very promising candidates for the adsorption of pollutants in water purification.

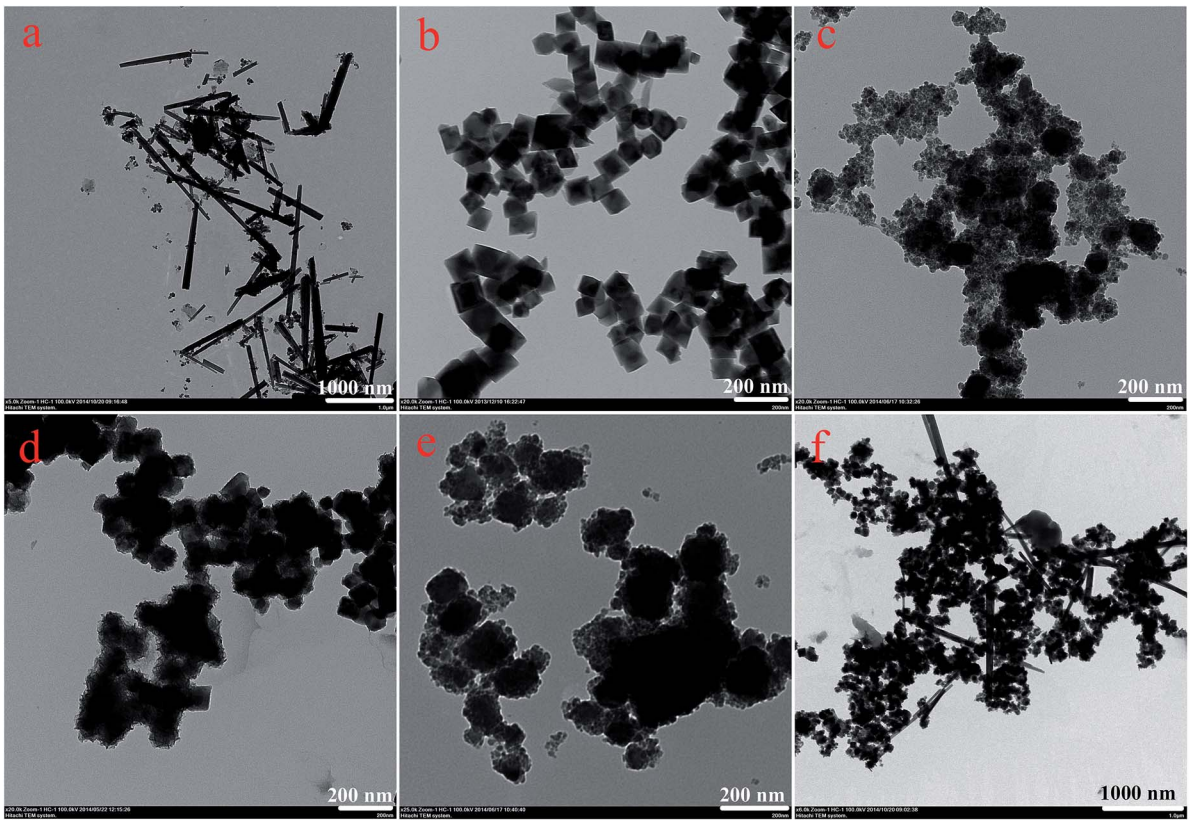

Fig. 2 TEM images of as-prepared nanostructures. (a), MnO_2; (b), Fe_3O_4; (c)–(f), Fe_3O_4@MnO_2 nanocomposites prepared at times of 3 h, 6 h, 9 h, and 15 h, respectively.

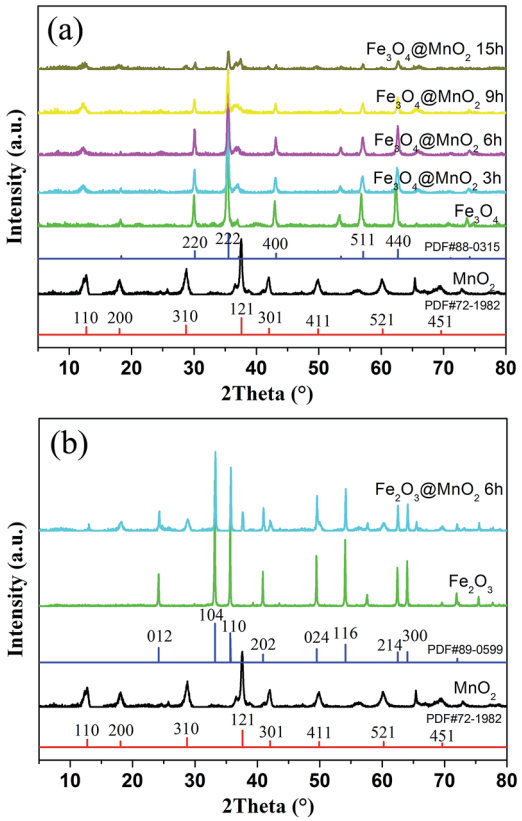

Fig. 3 XRD patterns of as-prepared MnO_2, Fe_3O_4@MnO_2 (a) and Fe_2O_3@MnO_2 (b) nanocomposites.

Fig. 4 displays the nitrogen adsorption–desorption isotherms and pore size distribution curves calculated by the Barrett–Joyner–Halenda (BJH) method. At low relative pressure (P/P_0 < 0.45), the adsorption and desorption curves coincide because of reversible monolayer adsorption. At a higher relative pressure region (P/P_0 0.45–0.95), all of the isotherms have significant hysteresis, which can be ascribed to the presence of a mesoporous structure in the interleaving nanoplates or cavities of the hollow spheres, and the hysteresis loop at $P/P_0 = 0.9$ to 1 could result from the internanorods space.[34,35] The specific surface area for each sample was obtained by the BET method. The physical properties deduced from N_2 adsorption at 77 K of as-prepared nanocomposites samples were listed in Table S1 in ESI.† The specific surface areas of MnO_2, Fe_3O_4@MnO_2, and Fe_2O_3@MnO_2 nanocomposites prepared at time of 6 h were 40.5, 72.5, and 52.2 $m^2\ g^{-1}$, respectively. The larger specific surface-area of Fe_3O_4@MnO_2 sample than that of Fe_2O_3@MnO_2 sample could be considered as the result of smaller particle diameter of Fe_3O_4 and more MnO_2 aggregate in shell part of sphere composites. The high specific surface area and the mesoporous nature of the hollow spheres and urchins can effectively absorb the dye, thus increasing the contact probability of pollutant molecule and catalyst. BJH analysis for mesopore distribution is also shown. The pore sizes of the MnO_2, Fe_3O_4@MnO_2, and Fe_2O_3@MnO_2 nanocomposites prepared upon 6 h are within the range of 7–16 nm, respectively.

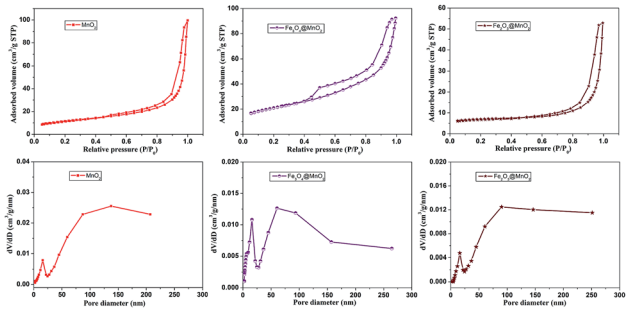

Fig. 4 The nitrogen adsorption–desorption isotherms and pore size distributions of as-prepared MnO_2, Fe_3O_4@MnO_2 and Fe_2O_3@MnO_2 nanocomposites samples at time of 6 h calculated by BJH method.

Fig. 5 demonstrates the hysteresis loops of Fe_3O_4/MnO_2 composites at room temperature. The saturation magnetization of the prepared Fe_3O_4 nanoparticles was 83.0 emu g^{-1}, which was more than the value reported for another pure Fe_3O_4 nanocrystals.[36] As for the Fe_3O_4@MnO_2 nanocomposites prepared upon 3 h, 6 h, 9 h, and 15 h reaction, respectively, the decrement tendency with time was clearly observed. The values of saturation magnetization were 74.2, 66.4, 36.6, and 18.5 emu g^{-1}, respectively. The decrease in the saturation magnetization with increasing hydrothermal treatment time can be attributed to the increase in the non-magnetic MnO_2 content in the composites with hydrothermal treatment time. However, this value was strong enough to achieve a facile magnetic separation. The as-prepared Fe_3O_4/MnO_2 composites were rapidly collected within seconds from an aqueous suspension by an external magnetic field. In addition, the separated particles were easily redispersed with gentle shaking to a fairly stable suspension. This is essentially important for the convenient reuse of composites.

The dye adsorption capacity was evaluated by placing the as-prepared Fe_3O_4@MnO_2 and Fe_2O_3@MnO_2 nanocomposites prepared at 6 h in MB and RhB aqueous solutions, respectively. The absorbance at 662 nm (for MB) and 554 nm (for RhB) was used to determine the concentration of residual dyes for samples collected at different time intervals. The

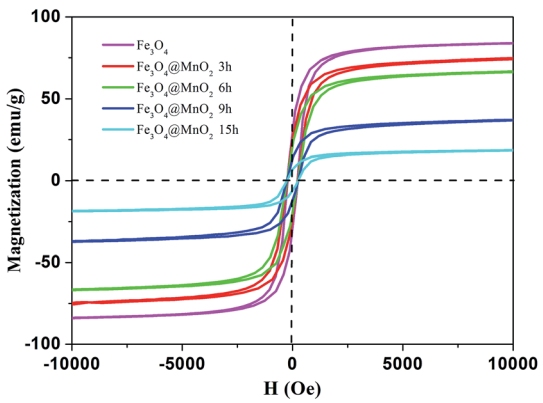

Fig. 5 Hysteresis loops of as-prepared Fe_3O_4 nanoparticle and Fe_3O_4@MnO_2 nanocomposites at different time intervals at 298 K.

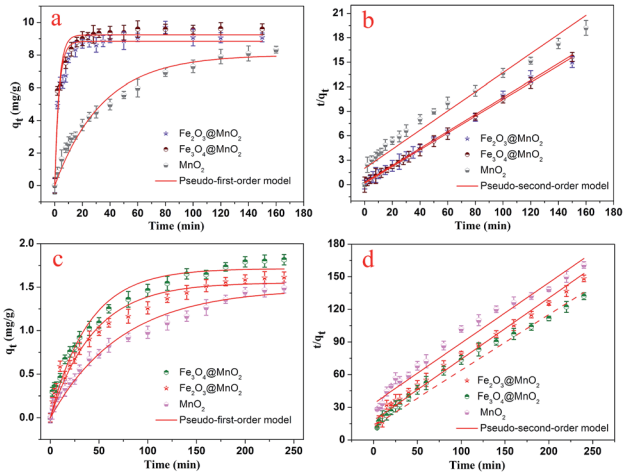

Fig. 6 Adsorption kinetics curves of as-prepared $Fe_3O_4@MnO_2$ and $Fe_2O_3@MnO_2$ nanocomposites onto MB (a and b) and RhB (c and d) at 298 K.

thermodynamic behaviors of the as-prepared nanocomposites for dye adsorption from aqueous solutions were reported and investigated in details,[19] and the results are shown in Fig. 6. The composites exhibit a continuous adsorption process, with equilibrium time of approximately 20 and 150 min for MB and RhB, respectively. The equilibrium time thus obtained is acceptable for efficient adsorption applications. Such kinetic behaviour can be also associated with the unique structure of nanocomposites, *i.e.*, the large three-dimensional interleaving thin nanoplates nanostructure as the adsorption sites.

The pseudo-first-order model:

$$\log(q_e - q_t) = \log q_e - \frac{k}{2.303}t \quad (1)$$

The pseudo-second-order model:

$$\frac{t}{q_t} = \frac{1}{kq_e^2} + \frac{t}{q_e} \quad (2)$$

where q_e and q_t represent the amount of dye adsorbed (mg g^{-1}) at equilibrium and time t, respectively, and the k_1 or k_2 values are the kinetic rate constants.[37,38] The kinetic data (Table S2 in ESI†) indicated that the pseudo-second-order model with a high correlation coefficient ($R^2 > 0.991$) seemed better to accurately describe present adsorption process than the pseudo-first-order model. In addition, from a practical/industrial point of view, the recycling and reuse of the adsorbent is an economic necessity. The design of stabilized MnO_2 nanocomposite materials and the relative applications is still a challenging problem in the near future. Taking into consideration that organic solvent exhibited a better solubility capacity for the dye molecules used in this study, ethylene glycol and ethanol treatment is likely to be a suitable approach for the regeneration of prepared nanocomposites. In this case, the used $Fe_3O_4@MnO_2$ nanocomposites were extracted from dye solutions through the external magnetic attraction, and washed alternatively using ethylene glycol and ethanol for several times. Finally, the

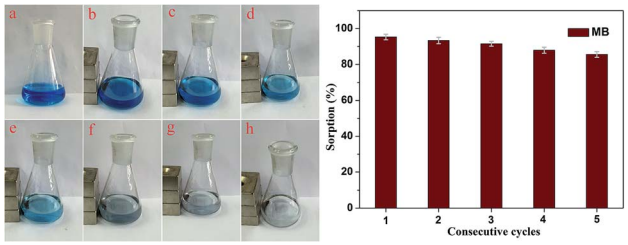

Fig. 7 Regeneration studies of as-prepared $Fe_3O_4@MnO_2$ nanocomposites in the removal of MB. The photographs showed the MB solution (a) and adsorption process under magnetic separation at different time intervals ((b)–(h) 0, 10, 20, 30, 40, 50, and 60 min).

regenerated core–shell composites were washed by DI water and dried in a lyophilizer for subsequent adsorption experiments.

The adsorption–desorption cycles for MB were repeated five times using the same batch of $Fe_3O_4@MnO_2$ nanocomposites prepared at 6 h, as shown in Fig. 7. As compared to the first adsorption, the removal efficiency at the fifth cycle decreased by about 9% to a value of 86%, indicating good regeneration capacity and reusability. The slight decrease in the adsorption capacity was attributed to the incomplete desorption of dyes from the surface of $Fe_3O_4@MnO_2$ nanocomposites. For MB molecules that go into the vacant site of MnO_2, desorption may be more difficult. After five cycles, the magnetic intensity of nanocomposites did not decrease and the adsorbent could be separated from solution rapidly. Overall, the prepared magnetic $Fe_3O_4@MnO_2$ composite can be easily recycled and reused several times, which supports their long term use in water purification.

4. Conclusions

In summary, two types of hollow hierarchical core–shell MnO_2 nanocomposites have been synthesized by a simple and facile hydrothermal method. The obtained novel sphere or urchin structured composites possess a high loosely mesoporous cluster structure consisting of thin plates and exhibit enhanced adsorption capacity for the dyes used in this study. The microstructures and good adsorption capability coupled with the low cost and environmentally benign nature of manganese may make these composite materials attractive for broad spectrum of applications. In addition, the magnetic $Fe_3O_4@MnO_2$ nanocomposite can be easily recycled and reused several times, which supports the long term use in water purification. Furthermore, the hydrothermal method has excellent reliability, selectivity, and efficiency for synthesizing inorganic materials with uniform and distinct morphologies.

Acknowledgements

This work was financially supported by the National Natural Science Foundation of China (grant nos 21473153 and 21207112), the Natural Science Foundation of Hebei Province (grant no. B2013203108), the Science Foundation for the Excellent Youth Scholars from Universities and Colleges of

Hebei Province (grant nos Y2011113, YQ2013026), the Support Program for the Top Young Talents of Hebei Province, and the Open Foundation of National Key Laboratory of Biochemical Engineering (Institute of Process Engineering, Chinese Academy of Sciences).

Notes and references

1 S. Dadfarnia, A. M. Haji Shabani, S. E. Moradi and S. Emami, *Appl. Surf. Sci.*, 2015, **330**, 85–93.
2 Y. R. Zhang, S. L. Shen, S. Q. Wang, J. Huang, P. Su, Q. R. Wang and B. X. Zhao, *Chem. Eng. J.*, 2014, **239**, 250–256.
3 Y. Wang, Z. Li, Y. He, F. Li, X. Q. Liu and J. B. Yang, *Mater. Lett.*, 2014, **134**, 115–118.
4 C. Namasivayam and D. Sangeetha, *J. Hazard. Mater.*, 2006, **135**, 449–452.
5 X. Peng, Z. Luan, J. Ding, Z. Di, Y. Li and B. Tian, *Mater. Lett.*, 2005, **59**, 399–403.
6 M. Gallego, Y. P. De Pena and M. Valcarcel, *Anal. Chem.*, 1994, **66**, 4074–4078.
7 R. Rostamian, M. Najafi and A. A. Rafati, *Chem. Eng. J.*, 2011, **171**, 1004–1011.
8 S. Mahdavi, M. Jalali and A. Afkhami, *Chem. Eng. Commun.*, 2013, **200**, 448–470.
9 D. Guo, W. J. Ren, Z. Chen, M. L. Mao, Q. H. Li and T. H. Wang, *RSC Adv.*, 2015, **5**, 10681–10687.
10 V. Yathindranath, M. Worden, Z. Z. Sun, D. W. Miller and T. Hegmann, *RSC Adv.*, 2013, **3**, 23722–23729.
11 M. N. Nadagouda, C. Bennett-Stamper, C. White and D. Lytle, *RSC Adv.*, 2012, **2**, 4198–4204.
12 Y. Liu, G. Su, B. Zhang, G. Jiang and B. Yan, *Analyst*, 2011, **136**, 872–877.
13 K. Mandel, F. Hutter, C. Gellermann and G. Sextl, *ACS Appl. Mater. Interfaces*, 2012, **4**, 5633–5642.
14 A. Farrukh, A. Akram, A. Ghaffar, S. Hanif, A. Hamid, H. Duran and B. Yameen, *ACS Appl. Mater. Interfaces*, 2013, **5**, 3784–3793.
15 S. Shin and J. Jang, *Chem. Commun.*, 2007, 4230–4232.
16 S. Shi, Y. Fan and Y. Huang, *Ind. Eng. Chem. Res.*, 2013, **52**, 2604–2612.
17 J. Zhu, S. Wei, H. Gu, S. B. Rapole, Q. Wang, Z. Luo, N. Haldolaarachchige, D. P. Young and Z. Guo, *Environ. Sci. Technol.*, 2011, **46**, 977–985.
18 J. F. Liu, Z. S. Zhao and G. B. Jiang, *Environ. Sci. Technol.*, 2008, **42**, 6949–6954.
19 X. Liu, Q. Hu, Z. Fang, X. Zhang and B. Zhang, *Langmuir*, 2008, **25**, 3–8.
20 J. E. Post, *Proc. Natl. Acad. Sci. U. S. A.*, 1999, **96**, 3447–3454.
21 T. Pal, R. Sahoo, M. Pradhan, A. Roy, S. Dutta, C. Ray, Y. Negishi and A. Pal, *Chem.–Asian J.*, 2015, DOI: 10.1002/asia.201500200, in press.
22 J. Zhu, S. A. Baig, T. Sheng, Z. Lou, Z. Wang and X. Xu, *J. Hazard. Mater.*, 2015, **286**, 220–228.
23 L. Tan, J. Wang, Q. Liu, Y. Sun, X. Jing, L. Liu, J. Liu and D. Song, *New J. Chem.*, 2015, **39**, 868–876.
24 Z. Zhao, J. Liu, F. Cui, H. Feng and L. Zhang, *J. Mater. Chem.*, 2012, **22**, 9052–9057.
25 E. J. Kim, C. S. Lee, Y. Y. Chang and Y. S. Chang, *ACS Appl. Mater. Interfaces*, 2013, **5**, 9628–9634.
26 Q. Han, Z. Wang, J. Xia, S. Chen, X. Zhang and M. Ding, *Talanta*, 2012, **101**, 388–395.
27 H. Jiao and J. Wang, *J. Alloys Compd.*, 2013, **577**, 402–408.
28 M. Xu, L. Kong, W. Zhou and H. Li, *J. Phys. Chem. C*, 2007, **111**, 19141–19147.
29 W. Ostwald, *Z. Phys. Chem.*, 1900, **34**, 495–503.
30 S. J. Bao, Q. L. Bao, C. M. Li, T. P. Chen, C. Q. Sun, Z. L. Dong, Y. Gan and J. Zhang, *Small*, 2007, **3**, 1174–1177.
31 B. Li, G. Rong, Y. Xie, L. Huang and C. Feng, *Inorg. Chem.*, 2006, **45**, 6404–6410.
32 H. G. Yang and H. C. Zeng, *J. Phys. Chem. B*, 2004, **108**, 3492–3495.
33 Y. Wang, Q. Zhu and H. Zhang, *Chem. Commun.*, 2005, 5231–5233.
34 Y. Tao, H. Kanoh, L. Abrams and K. Kaneko, *Chem. Rev.*, 2006, **106**, 896–910.
35 Y. Meng, D. Chen and X. Jiao, *J. Phys. Chem. B*, 2006, **110**, 15212–15217.
36 D. Caruntu, G. Carnutu and C. J. O'Connor, *J. Phys. D: Appl. Phys.*, 2007, **40**, 5801–5809.
37 Q. Zhang, Z. Zhang, J. Teng, H. Huang, Q. Peng, T. Jiao, L. Hou and B. Li, *Ind. Eng. Chem. Res.*, 2015, **54**, 2940–2949.
38 Q. Zhang, Q. Du, T. Jiao, B. Pan, Z. Zhang, Q. Sun, S. Wang, T. Wang and F. Gao, *Chem. Eng. J.*, 2013, **221**, 315–321.